Available online at www.sciencedirect.com
ScienceDirect
Nuclear Instruments and Methods in Physics Research B 264 (2007) 361–370
NIM B
Beam Interactions with Materials & Atoms
www.elsevier.com/locate/nimb

An analytic formalism for the emission of coherent transition radiation from an oblique finite thin metallic target screen

Daniel Sütterlin [a,b,*,1], Daniel Erni [c], Micha Dehler [b], Heinz Jäckel [d], Hans Sigg [b], Volker Schlott [b]

[a] PUBLICA Swiss Federal Pension Fund, CH-3000 Berne, Switzerland
[b] Paul Scherrer Institute, CH-5232 Villigen, Switzerland
[c] General and Theoretical Electrical Engineering (ATE), Faculty of Engineering, University of Duisburg-Essen, D-47048 Duisburg, Germany
[d] Electronics Laboratory, ETH Zürich, CH-8092 Zürich, Switzerland

Received 5 November 2006; received in revised form 28 July 2007
Available online 18 September 2007

Abstract

Long-wavelength coherent transition radiation is commonly used in electron beam diagnostics for the determination of bunch lengths. Typically the spectrum of coherent transition radiation for a short bunch accelerator is settled in the low or sub-THz regime. Hereby, we present a theoretical model based on physical optical techniques in order to calculate emission characteristics for transition radiation, for both the radiating near-field and the far-field. This approach yields analytic solutions for the emitted electromagnetic fields without the need to solve integral equations. The simulated intensity distribution is compared with measurements showing good agreement.

PACS: 29.17.+w; 84.40.x; 61.80.Fe; 29.27.a; 41.75.Ht

Keywords: Coherent transition radiation; Linear accelerator; Electron bunch length; THz radiation

1. Introduction

The well-known relation derived by Ginzburg and Frank for transition radiation (TR) predicts frequency independent symmetrical emission characteristics [1,2]. This result is valid only when the source fields impinging onto the radiating screen are of considerably smaller extent ($\gamma\lambda$) than the target dimension, which is typically the case in the optical range of the spectrum.

Several approaches have been pursued to describe the generation of TR. Generally one can distinguish three different perceptions for the emission process. A prominent one is the model of the virtual quanta [3] which is based on the assumption of virtual photons, constituting the electromagnetic source fields of the particle, which are converted into real photons by reflection at the finite metallic interface. Prerequisite for this model is the fact that the electromagnetic field of a highly relativistic electron in the laboratory frame is confined in a flat disk perpendicular to the direction of motion. Hence, this yields only tangential fields as required in the approach. Here it is taken full advantage of the boundary condition that the tangential electrical field E_t at the boundary of a perfect electrical conductor (PEC) must vanish. This necessitates a change in sign of the incoming to the outgoing electrical field, which thus corresponds to the reflection of the incident wave at the metallic target interface [4,5].

However, this scheme can also be applied for a tilted screen where the normal projections of the tangential fields mediate the change in sign of the outgoing wave but which is then reflected in another direction as the incident wave.

* Corresponding author. Address: PUBLICA Swiss Federal Pension Fund, CH-3000 Berne, Switzerland.
E-mail address: daniel.suetterlin@publica.ch (D. Sütterlin).
[1] Supported by the Swiss National Science Foundation (SNF).

0168-583X/$ - see front matter © 2007 Elsevier B.V. All rights reserved.
doi:10.1016/j.nimb.2007.08.092

The second approach for the generation of TR is that of the moving mirror charge [1]. Here the electron and its mirror-(anti) particle which is incident from the opposite side of the target are stopped abruptly at the screen boundary while their charge is annihilated. In this view only their electromagnetic fields are remaining which thus can be identified as radiation from the target. A more realistic perception than charge annihilation is that of Bremsstrahlung [6]. Similar to the annihilation model the relativistic electron is abruptly stopped at the target. In accordance with the fundamental principle of energy conservation the kinetic energy of the electron is emitted as radiation which can be identified as TR.

In this paper we introduce a fourth view for the generation of transition radiation in which the metallic target screen itself is considered as source of the radiation using the so-called Physical–Optics (PO) technique [7,8]. In this perception the magnetic field of the relativistic electron induces surface current density $\vec{j}_s$ in the finite circular metallic target, from which the vector potential representation of the radiated field is acquired. The use of the well-known PO approach yields an analytical solution for the electromagnetic fields of the emitted TR. Thus, it represents a very fast method for the calculation of the emerging fields, without the need to solve integral equations. When calculating the components of the resulting electrical and magnetic fields a further formalism has been introduced that provides accurate approximations for both cases the far-field and the radiating near-field. Similar to the model of the virtual quanta only the backward TR emission is considered.

The derivation of TR emission using the virtual quanta model is based on scalar Kirchhoff diffraction theory. However, we will show, that due to the redundancy of the PEC boundary conditions both models are equivalent. In contrast our model introduces a descriptive presentation of the generation mechanism of TR which is based on a vectorial formalism and which allows the computation of TR as obtained even from rough and uneven surfaces [9].

Since standard diagnostic ports use targets rotated by $\pi/4$ into the electron beam path, a circular tilted radiator is considered. The induced surface currents corresponds to the boundary condition for the magnetic field, which may become redundant to the one of the electrical field in the case where a perfect electrical conducting (PEC) target interface is assumed.

The far-field condition $L \gg \gamma^2\lambda$ for the radiating target as given by comprehensive references [4,5] yields distances up to several hundreds of meters for TR in the FIR region. This is a consequence of the source fields, which transversal extent is given by $d = \gamma\lambda$. In our description the transition from the near-field to the far-field zone is characterized by the Rayleigh distance, which is approximated according to $L_R = 4r_s^2/\lambda$ where r_s stands for the radius of the radiating screen. It is worth noting that in the limiting case where the target size ($d = 2r_s$) equals the transversal extend of the source field ($\gamma\lambda$) the two descriptions for the far-field criterion converge.

The remainder of the paper is organized as follows. In the second section an electromagnetic description for the source field formation induced by the relativistic electron passage through the target is introduced. Based on this electromagnetic source term a closed form expression for the backward coherent transition radiation (CTR) from an oblique target screen is then presented in the third section. The introduced formalism yields accurate results for the wave zone (or the far-field, i.e. for the observation points farther than the Rayleigh distance) and provides very good approximations for the radiating near-field (or the Fresnel zone, i.e. for observation points within the Rayleigh distance), both for finite targets with lateral sizes that may become even smaller than the transversal extent $\gamma\lambda$ of the relativistic electron's Coulomb-field Fourier-component. A proper validation of the emission formalism is given in the fourth section along with a typical test example: This confirms the asymmetric emission characteristic occurring for the horizontal polarized CTR lobes. This asymmetry predicted by the formalism was experimentally confirmed at the pre-injector LINAC of the Swiss Light Source (SLS) [10,11]. Finally the contribution concludes in the fifth section with a short summary.

2. Electromagnetic fields of relativistic electrons

For a relativistic electron which rest frame moves in free space along the z-axis in respect to the laboratory frame we define the longitudinal Fourier transform by:

$$\hat{A}(\omega) = \int_{-\infty}^{+\infty} A(\eta)\cdot \mathrm{e}^{-i\eta\omega}\mathrm{d}\eta = \mathrm{e}^{\mathrm{i}\omega\frac{z}{\beta c}}\cdot \int_{-\infty}^{+\infty} A(t)\cdot e^{-i\omega t}\mathrm{d}t \quad (1)$$

with the longitudinal coordinate $\eta = t - \frac{z}{v} = t - \frac{z}{\beta c}$.

It is convinient to consider the problem in cylindrical coordinates. From symmetry only the radial and longitudinal components of the electric field (E_r and E_z) and the azimuthal components of the magnetic field (B_ϕ) have to be considered. In vacuum with $\vec{D} = \epsilon_0\vec{E}$ and $\vec{B} = \mu_0\vec{H}$ the macroscopic Maxwell equations in cylindrical coordinates are written as follows:

$$\frac{1}{r}\partial_r(rE_r) + \partial_z E_z = \frac{\rho}{\varepsilon_0} \quad (2)$$

$$\frac{1}{r}\partial_\phi B_\phi = 0 \quad (3)$$

$$frac1r\partial_\phi E_z = 0 \quad (4)$$

$$\partial_z E_r - \partial_r E_z = -\partial_t B_\phi \quad (5)$$

$$\frac{1}{r}\partial_\phi E_r = 0 \quad (6)$$

$$-\partial_z B_\phi = \frac{1}{c^2}\partial_t E_r \quad (7)$$

$$\frac{1}{r}\partial_r(rB_\phi) = \mu_0 j_z + \frac{1}{c^2}\partial_t E_z \quad (8)$$

where ρ denotes the charge density and the current $\vec{j}$ has only a longitudinal component originating from the

moving charge distribution. Applying the above defined Fourier transform (1) to Maxwell's equations yields:

$$\frac{1}{r}\partial_r(r\hat{E}_r)+\frac{i\omega}{\beta c}\hat{E}_z=\frac{\hat{\rho}}{\varepsilon_0} \tag{9}$$

$$\frac{1}{r}\partial_\phi\hat{B}_\phi=0 \tag{10}$$

$$\frac{1}{r}\partial_\phi\hat{E}_z=0 \tag{11}$$

$$\frac{i\omega}{\beta c}\hat{E}_r-\partial_r\hat{E}_z=i\omega\hat{B}_\phi \tag{12}$$

$$\frac{1}{r}\partial_\phi\hat{E}_r=0 \tag{13}$$

$$-\frac{i\omega}{\beta c}\hat{B}_\phi=-\frac{i\omega}{c^2}\hat{E}_r \tag{14}$$

$$\frac{1}{r}\partial_r(r\hat{B}_\phi)=\mu_0\hat{j}_z-\frac{i\omega}{c^2}\hat{E}_z \tag{15}$$

Maxwell's equations are then solved in Fourier space obtaining the Fourier-components of the magnetic field which are given by [5]

$$\hat{B}_\phi=\frac{q}{(2\pi)^{1/2}\epsilon_0\beta^2 c}\frac{\omega}{c\gamma}\cdot K_1\left(\frac{\omega}{\beta\ c\gamma}r\right), \tag{16}$$

where K_1 is the modified Bessel function of first order. From Eq. (14) it follows directly that

$$\hat{E}_r=\frac{q}{(2\pi)^{1/2}\epsilon_0\beta^2 c}\frac{\omega}{\beta\gamma}\cdot K_1\left(\frac{\omega}{\beta\ c\gamma}r\right). \tag{17}$$

The longitudinal component is obtained by inserting Eqs. (16) and (17) into (12)

$$\begin{aligned}\partial_r\hat{E}_z &\propto \frac{i\omega}{\beta c}\frac{\omega}{\beta\gamma}\cdot K_1\left(\frac{\omega}{\beta\ c\gamma}r\right)-i\omega\frac{\omega}{c\gamma}\cdot K_1\left(\frac{\omega}{\beta\ c\gamma}r\right)\\ &=\frac{i(\omega)^2}{c\gamma\beta^2}\cdot K_1\left(\frac{\omega}{\beta\ c\gamma}r\right)(1-\beta^2)=\frac{i(\omega)^2}{c\gamma^3\beta^2}\cdot K_1\left(\frac{\omega}{\beta\ c\gamma}r\right).\end{aligned} \tag{18}$$

For simplicity we have neglected here the pre-factor. With $\partial_r(K_0(a\,r))=-a\cdot K_1(a\,r)$ and by inserting the pre-factor the longitudinal component is readily calculated:

$$\hat{E}_z=-\frac{i\omega}{\gamma^2\beta}\frac{q}{(2\pi)^{1/2}\epsilon_0\beta^2 c}\cdot K_0\left(\frac{\omega}{\beta\ c\gamma}r\right). \tag{19}$$

For typical kinetic energies of some hundred MeV the γ-factor becomes large and the longitudinal component $\hat{E}_z$ can therefore be neglected. Thus, it indicates that the electromagnetic field is confined in a disk perpendicular to the direction of motion. In the laboratory frame the longitudinal components are contracted by a factor of γ with respect to the transverse/tangential field components: $\hat{E}_r,\hat{B}_\phi\propto 1/\gamma$, $\hat{E}_z\propto 1/\gamma^2$.

Fig. 1 depicts two plots of the radial electrical field $r\cdot\hat{E}_r(r)$ (due to the Jacobian for the cylindrical coordinate transform) for different values of the relativistic Lorentz factor γ. For each γ the fields are computed for five different wavelengths ($\lambda=0.$ mm, 0.5 mm, 1.0 mm, 2.0 mm and 5.0 mm). For large wavelengths the fields are nearly constant over the radius of the screen. The effect is becoming more dominant for higher values of γ. Since, $\hat{B}_\varphi=(\beta/c)\hat{E}_r$ the same behavior applies for the magnetic field.

3. Transition radiation emitted from an oblique target screen

A standard TR diagnostic port consists of a target screen rotated by an angle of $\pi/4$ to the direction of the electron beam allowing the extraction of the backward TR through a vacuum window. In the following a tilted circular thin metallic screen representing the radiating source is considered. Most important the metallic target screen itself is treated as a source of the emitted TR using the Physical–Optics (PO) approach. The PO technique is a well-known and widely used optical approximate technique for the calculation of the electromagnetic field scattered from a perfectly conducting (PEC) surface by an incident electromagnetic field. It is a very fast method since it does not require an integral equation to be solved. The idea is to approximate the surface currents $\vec{j}_s$ induced by the incident magnetic fields $\vec{H}_{(inc)}$ which then represents the source term in the inhomogeneous Helmholtz equation describing the propagation of the resulting vector potential $\vec{A}$.

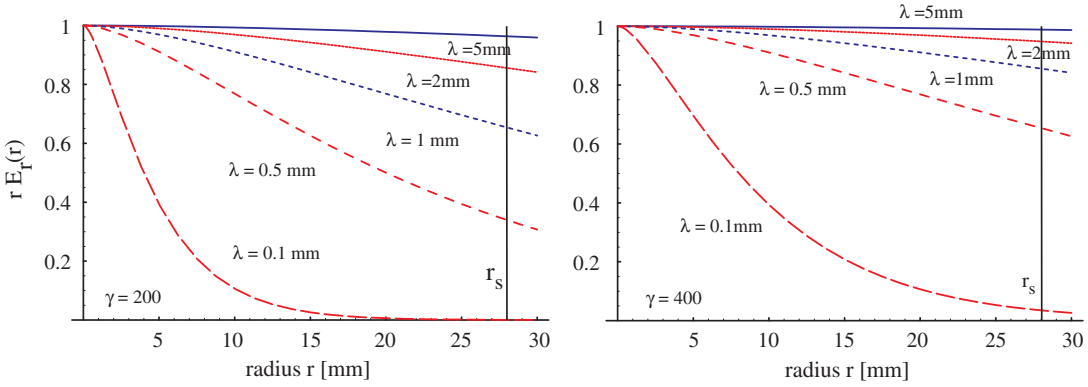

Fig. 1. The radial field $r\cdot\hat{E}_r(r)$ (due to the Jacobian for the cylindrical coordinate transform) for different wavelengths and two different γ values.

Assuming a PEC target physically means that the fields do not penetrate into the conductor. Even for realistic metallic conductors one obtains skin depths in the order of 100 nm [12] which compares only to tiny a fraction of the wavelength involved ($\lambda = 1$ mm). The conductor can therefore be assumed to be field-free, and, hence, only reflected fields are generated in the framework of the virtual quanta model. The connection to PO is revealed along the boundary conditions, which provides an exact measure of the surface current, i.e. for the source term of the backward TR.

3.1. PEC boundary conditions

We start with the well-known boundary conditions at the interface of a dielectric medium i adjacent to a PEC

$$\vec{E}_{\mathrm{it}} = \vec{0} \tag{20}$$

$$\vec{H}_{\mathrm{it}} = \vec{j}_{\mathrm{s}} \wedge \vec{n} \tag{21}$$

$$\epsilon \vec{E}_{\mathrm{in}} = \zeta \tag{22}$$

$$\mu \vec{H}_{\mathrm{in}} = 0 \tag{23}$$

where ζ is the surface charge density, n labels the field component normal to the interface, $\vec{n}$ denotes the normal unit vector directed into region i, index t labels the tangential field component and $\vec{j}_{\mathrm{s}}$ is the surface current density, which can be retrieved by inverting Eq. (21)

$$\vec{j}_{\mathrm{s}} = \vec{n} \wedge \vec{H}_{\mathrm{it}} \tag{24}$$

In case of unknown surface currents and charge densities and while assuming the non-static case only condition (20) is required. Condition (21) and hence Eq. (24) will act as a proper definition for the unknown surface current. As the electromagnetic field of the relativistic electron has negligible longitudinal field components i.e. comprising only the transversal polarization, condition (20) has to be satisfied. This yields total electrical field $\vec{E}_{(\mathrm{tot})}$ to become zero at the PEC interface and renders the outgoing wave $\vec{E}_{(\mathrm{sc})}$ to be a reflected one with $\vec{E}_{(\mathrm{sc})} = -\vec{E}_{(\mathrm{inc})}$ having an inverted polarization direction. Again, this is tantamount to the picture of the virtual quanta where the electromagnetic field of the relativistic electron is set equivalent to an electromagnetic pulse that afterwards may undergo total specular reflection at the target screen.

3.2. Surface currents induced by the magnetic field

For the transversal magnetic field the contributions from the incident and the totally reflected wave fields-namely $\vec{H}_{(\mathrm{inc})}$ and $\vec{H}_{(\mathrm{sc})}$ will equally sum up to form $\vec{H}_{(\mathrm{tot})}$, which according to (24) induces the source current density for the PO approach.

$$\vec{j}_{\mathrm{s}} = \vec{n} \wedge \vec{H}_{(\mathrm{tot})} = 2\vec{n} \wedge \vec{H}_{(\mathrm{inc})} \tag{25}$$

Since everything is linear, this generalizes to target planes other than $z = 0$, i.e. tilted target screens where e.g. normal projections of the transversal electrical field on the target interface emerge. The normal components only mediate the sign reversal in the tangential field projections with respect to the oblique incident virtual quanta and its corresponding reflection. Dealing with a PEC interface has thus revealed a sort of redundancy: Both boundary conditions for the electrical field are surplus relations if the emerging TR is modeled using solely the magnetic field (and its corresponding boundary condition) where the resulting surface current density is the proper source of TR. But then enforcing the boundary conditions for the electrical field components only has led us to the independent model of e.g. virtual quanta. In the case of a general target material (i.e. non PEC material) the redundancy is removed and always two types of boundary conditions have to be taken into account.

3.3. Vector potential representation

In the target the resulting surface current densities $\vec{j}_{\mathrm{s}}$ are acting as electric current sources from which a vector potential[2] $\vec{A}$ for the radiated field can be determined:

$$\mathrm{d}\vec{A} = \frac{\mu_0}{4\pi} \cdot \vec{j} \cdot \frac{\mathrm{e}^{\mathrm{i}\frac{\omega}{c}R}}{R} \mathrm{d}S \qquad \text{with} \quad \mathrm{d}S = r' \mathrm{d}r' \mathrm{d}\phi' \tag{26}$$

R is the distance from a point $\vec{r}'_{\mathrm{s}} = (x', y', z')$ on the target screen to a point of observation $\vec{r}_{\mathrm{obs}} = \rho \cdot \vec{e}_{\rho}$ (see Fig. 2). Here we have used the fact, that the vector potential $\vec{A}$ does satisfy the inhomogeneous Helmholtz equation, which describes the propagation of the vector potential. The solution to the inhomogeneous Helmholtz equation is given by the superposition of the spherical waves $\mathrm{e}^{\mathrm{i}(\omega/c)R}/R$.

3.4. Edge effects and multiple reflections

Within the framework of our source model we have assumed an anechoic behavior for the induced currents at the screen boundaries. However, possible fringe effects could be considered by applying a modified surface current density calculated by perturbation theory, but noteworthy without changing our formalism. However, in contrast to the analytical solution presented here, this necessitates a numerical approach, rendering the formalism much more complex.

An additional question may arise with respect to temporal perturbations that could be caused by a potential surface (current) wave resonance on the finite target screen. There are several arguments against this conjecture. First, the PEC like target barely supports surface waves. Second, referring to the scattering model (i.e. the model of virtual quanta) a finite-sized target would only be excited through the target edges; hence, the strength of the resulting temporal perturbation is below the order of magnitude of the aforementioned edge effects. In turn a potential distortion of the outgoing wave must be radiated by the sides of the

[2] The vector potential $\vec{A}$ is defined by $\vec{B} = \vec{\nabla} \wedge \vec{A}$.

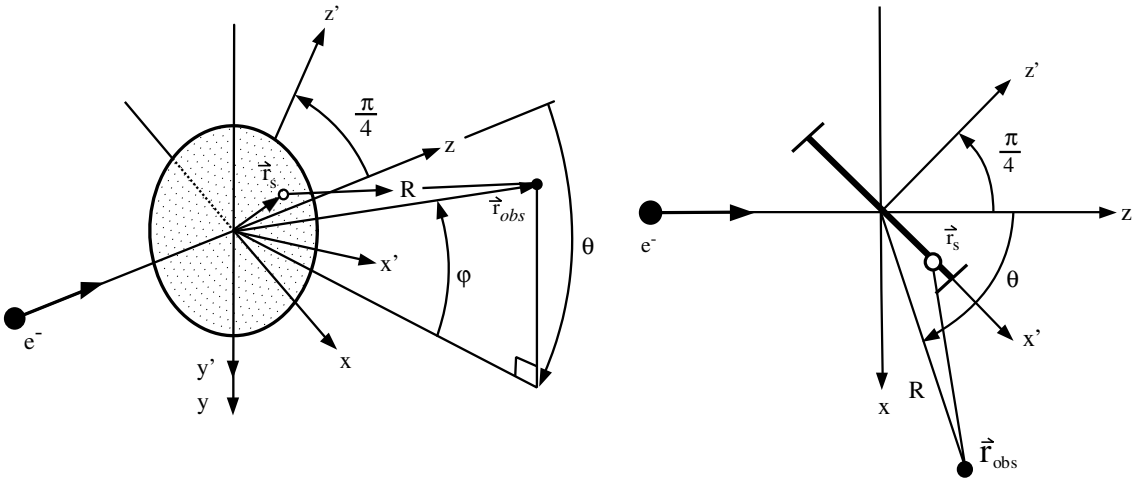

Fig. 2. Left side: schematic for the target geometry. The point of observation is given by $\vec{r}_{\mathrm{obs}}$ and parametrized by spherical coordinates (ρ, θ, φ). It is convenient to use polar coordinates (r', ϕ') for describing the position $\vec{r}_{\mathrm{s}}$ on the tilted screen. Right side: top-view of the target screen.

screen. Thus, a possible perturbation can only be a second order effect of the already small coupling efficiency. The third rationale is displayed within the proposed model. Here, the surface current density is induced virtually instantaneously in the PEC, while the generation of the current density by the magnetic fields happens on a very short timescale due to the fact that the electromagnetic fields of the relativistic electron are confined into a flat disk perpendicular to the direction of motion. Therefore, we can presume that the stimulation is too short compared to its strength to efficiently excite potential resonant surface waves within the finite target screen.

Mutual interactions namely multiple reflections at the metallic target screen can be neglected. This is mainly due to the fact, that we are dealing with a plane metallic scatterer which hardly causes multiple reflections (meaning that a scattered field might be reflected at another point of the surface again). Here we only have to consider the main reflection at the target screen ($\vec{H}_{\mathrm{inc}} \rightarrow \vec{H}_{\mathrm{sc}}$) Hence, this justifies the PO approach used in our model.

3.5. Coordinate transformation: π/4 rotation of the target screen

In order to determine the TR from a tilted target the screen is parametrized according to Fig. 2:

$$x' = r'\cos(\phi') \tag{27}$$

$$y' = r'\sin(\phi') \tag{28}$$

$$z' = 0 \tag{29}$$

The original coordinates are obtained from the screen coordinates by a π/4 rotation around the y'-axis:

$$x = \frac{1}{\sqrt{2}}x' \tag{30}$$

$$y = y' \tag{31}$$

$$z = \frac{1}{\sqrt{2}}x' \tag{32}$$

The transversal plane normal to the electron trajectory is described with the following polar coordinates (r,ϕ); $x = r\cos(\phi)$, $y = r\sin(\phi)$:

$$r(r',\phi') = \sqrt{x^2+y^2} = \sqrt{\frac{1}{2}(r'\cos(\phi'))^2 + (r'\sin(\phi'))^2} \tag{33}$$

$$\begin{aligned}\phi(r',\phi') &= \arg(x + i\cdot y)\\ &= \arg\left(\frac{1}{\sqrt{2}}r'\cos(\phi') + i\cdot r'\sin(\phi')\right).\end{aligned} \tag{34}$$

Due to the strong longitudinal confinement of the relativistic electron's field, the magnetic field will hit the π/4-tilted target at continuous subsequent positions z_1, z_2, ... where surface current densities $\vec{j}_s$ are then induced at the associated time delays t_1, t_2,.... The moving impact position as well as the associated impact time are characterized by a phase relation which is interrelated to the target screen's coordinate transformation. Therefore, we set the phase on the screen at position z to $\Psi(z) = \mathrm{e}^{\mathrm{i}\frac{\omega}{\beta c}z}$. The Fourier-components of the magnetic field on the screen are given by Eq. (16) multiplied with the phase term $\Psi(z)$ leading to:

$$\begin{aligned}\hat{B_\phi} &= \frac{q}{(2\pi)^{1/2}\epsilon_0\beta^2 c}\frac{\omega}{c\gamma}\mathrm{e}^{\mathrm{i}\frac{\omega}{\beta c}z}K_1\left(\frac{\omega}{\beta\, c\gamma}r\right)\\ &= \frac{q}{(2\pi)^{1/2}\epsilon_0\beta^2 c}\frac{\omega}{c\gamma}\mathrm{e}^{\mathrm{i}\frac{\omega}{\beta c}\frac{1}{\sqrt{2}}r'\cos(\phi)}K_1\left(\frac{\omega}{\beta\, c\gamma}r(r',\phi')\right).\end{aligned} \tag{35}$$

The x and y components are then:

$$\begin{aligned}\hat{B_x} &= -\sin(\phi(r',\phi'))\frac{q}{(2\pi)^{1/2}\epsilon_0\beta^2 c}\\ &\quad\times\frac{\omega}{c\gamma}\mathrm{e}^{\mathrm{i}\frac{\omega}{\beta c}\frac{1}{\sqrt{2}}r'\cos(\phi')}K_1\left(\frac{\omega}{\beta\, c\gamma}r(r',\phi')\right)\end{aligned} \tag{36}$$

$$\begin{aligned}\hat{B_y} &= \cos(\phi(r',\phi'))\frac{q}{(2\pi)^{1/2}\epsilon_0\beta^2 c}\\ &\quad\times\frac{\omega}{c\gamma}\mathrm{e}^{\mathrm{i}\frac{\omega}{\beta c}\frac{1}{\sqrt{2}}r'\cos(\phi')}K_1\left(\frac{\omega}{\beta\, c\gamma}r(r',\phi')\right).\end{aligned} \tag{37}$$

With $\hat{\vec{j}} = 2 \cdot \vec{n} \wedge \hat{\vec{H}}$ following the PO approach the components of the current density indexsurface current density induced by the magnetic field are calculated according to:

$$\mu_0 \hat{j}_x = -\frac{2}{\sqrt{2}} \hat{B}_y \tag{38}$$

$$\mu_0 \hat{j}_y = \frac{2}{\sqrt{2}} \hat{B}_x \tag{39}$$

$$\mu_0 \hat{j}_z = -\frac{2}{\sqrt{2}} \hat{B}_y. \tag{40}$$

As a next step we express the radiated field at an observation point $\vec{r}_{obs} = (\rho, \theta, \varphi)$ by the vector potential. For large distances ρ from the screen compared to the screen radius ($\rho \gg r$) the vector potential in spherical coordinates is thus expressed using Eq. (26) in conjunction with the transformation from cartesian to spherical coordinates:

$$\vec{e}_\rho = \sin(\theta)\cos(\varphi)\vec{e}_x + \sin(\theta)\sin(\varphi)\vec{e}_y + \cos(\theta)\vec{e}_z \tag{41}$$

$$\vec{e}_\theta = \cos(\theta)\cos(\varphi)\vec{e}_x + \cos(\theta)\sin(\varphi)\vec{e}_y - \sin(\theta)\vec{e}_z \tag{42}$$

$$\vec{e}_\varphi = -\sin(\varphi)\vec{e}_x + \cos(\varphi)\vec{e}_y \tag{43}$$

$$\begin{aligned} \mathrm{d}\hat{\vec{A}} = \frac{\mu_0}{4\pi}\frac{\mathrm{e}^{ik\rho}}{\rho}\big(&\cos(\varphi)\sin(\theta)\hat{j}_x + \sin(\theta)\sin(\varphi)\hat{j}_y \\ &+ \cos(\theta)\hat{j}_z, \cos(\theta)\cos(\varphi)\hat{j}_x + \cos(\theta)\sin(\varphi)\hat{j}_y \\ &- \sin(\theta)\hat{j}_z, -\sin(\varphi)\hat{j}_x + \cos(\varphi)\hat{j}_y\big)\mathrm{d}S. \end{aligned} \tag{44}$$

Here we have used the wavenumber $k = \omega/c$.

The magnetic induction $\vec{B} = (\hat{B}_\rho, \hat{B}_\theta, \hat{B}_\varphi)$ is found according to $\vec{B} = \mathrm{rot}(\vec{A})$.

$$\begin{aligned} \mathrm{d}\hat{\vec{B}} = \frac{\mu_0}{4\pi}\Bigg(0, &\frac{\mathrm{e}^{\mathrm{i}k\rho}}{\sin(\theta)\rho}\Bigg(-\mathrm{i}k\sin(\theta)(\cos(\varphi)\hat{j}_y - \sin(\varphi)\hat{j}_x) \\ &+ \frac{\sin(\theta)(\cos(\varphi)\hat{j}_y - \sin(\varphi)\hat{j}_x)}{\rho}, \frac{\mathrm{e}^{\mathrm{i}k\rho}}{\rho}(ik(\cos(\theta) \\ &\times \cos(\varphi)\hat{j}_x - \sin(\theta)\hat{j}_z + \cos(\theta)\sin(\varphi)\hat{j}_y)) \\ &- \frac{\cos(\theta)\cos(\varphi)\hat{j}_x - \sin(\theta)\hat{j}_z + \cos(\theta)\sin(\varphi)\hat{j}_y}{\rho}\Bigg)\Bigg)\mathrm{d}S \end{aligned} \tag{45}$$

Taking only the first order terms $\frac{1}{\rho}$ into account, the above expression simplifies to:

$$\begin{aligned} \mathrm{d}\hat{\vec{B}} \approx \frac{\mu_0}{4\pi}\Bigg(0, &\frac{\mathrm{e}^{\mathrm{i}k\rho}}{\sin(\theta)\rho}\Bigg(-ik\sin(\theta)(\cos(\varphi)\hat{j}_y \\ &- \sin(\varphi)\hat{j}_x), \frac{\mathrm{e}^{ik\rho}}{\rho}(ik(\cos(\theta)\cos(\varphi)\hat{j}_x - \sin(\theta)\hat{j}_z \\ &+ \cos(\theta)\sin(\varphi)\hat{j}_y))\Bigg)\Bigg)\mathrm{d}S \end{aligned} \tag{46}$$

The electric field $\hat{\vec{E}}$ is computed by:

$$\hat{\vec{E}} = \frac{1}{ick\epsilon_0}\mathrm{rot}(\hat{\vec{H}}) = \frac{1}{ick\epsilon_0\mu_0}\mathrm{rot}(\hat{\vec{B}}). \tag{47}$$

Referring to the aforementioned first order approximation, the field $\hat{\vec{E}}$ is thus written as

$$\mathrm{d}\hat{E}_\rho = 0 \tag{48}$$

$$\begin{aligned} \mathrm{d}\hat{E}_\theta \approx \frac{k}{4\pi}\frac{1}{ic\epsilon_0}\frac{\mathrm{e}^{ik\rho}}{\rho}&(\cos(\theta)\cos(\varphi)\hat{j}_x - \sin(\theta)\hat{j}_z \\ &+ \cos(\theta)\sin(\varphi)\hat{j}_y)\mathrm{d}S \end{aligned} \tag{49}$$

$$\mathrm{d}\hat{E}_\varphi \approx \frac{k}{4\pi}\frac{1}{ic\epsilon_0\mu_0}\frac{e^{ik\rho}}{\rho}(\cos(\varphi)\hat{j}_y - \sin(\varphi)\hat{j}_x)\mathrm{d}S \tag{50}$$

Eqs. (48) to (50) and (46) give an analytic electromagnetic field description of backward TR as emitted from an oblique, thin metallic target screen. The field components are calculated by integrating the above expressions over the thin circular target screen.

The spectral energy flux of the emitted radiation is calculated from the Pointing vector. Expressing the magnetic field $\vec{H}$ through the electrical field $\vec{E}$ [5] yields that the spectral energy flux at the point of observation must be proportional to the module square of the transverse electrical field $\vec{E}$. Using Parseval's theorem and $\mathrm{d}S = r'\mathrm{d}\phi'\mathrm{d}r'$ we finally get

$$\frac{\mathrm{d}^2 I}{\mathrm{d}\nu\mathrm{d}\Omega} \propto |\hat{\vec{E}}|^2 = \left|\int_0^{r_s}\int_0^{2\pi}(\mathrm{d}\hat{\vec{E}}_\theta + \mathrm{d}\hat{\vec{E}}_\varphi)\right|^2 \tag{51}$$

3.6. On simplification and error estimation

In order to define a range of validity of the developed formalism, a detailed error estimation and discussion including the applied assumptions, will be presented.

3.6.1. Phase error

In Eq. (44) we have used the simplification $R \approx \rho$ by inferring that $\rho \gg r$.

Considering the function $f(x_1, \ldots, x_n) = h(x_1, \ldots, x_n) \cdot \mathrm{e}^{g(x_1,\ldots,x_n)}$, where h and g are non-exponential functions, it follows that $\partial_{x_l} f = e^g(\partial_{x_l} h + h\partial_{x_l} g)$. Hence it must be that $\mathrm{rot}(\vec{A}) \propto \mathrm{e}^{\mathrm{i}kR(\rho,\theta,\varphi)}$ with $\mathrm{e}^{\mathrm{i}kR(\rho,\theta,\varphi)}$ being the sole exponential term. Therefore the inferred constraint is dramatically relaxed by allowing to substitute $\mathrm{e}^{\mathrm{i}k\rho}$ with $\mathrm{e}^{\mathrm{i}kR}$ in the final expression for the Fourier-components of the electrical field, where the exact distance R is given by the following expression:

$$\begin{aligned} R &= \sqrt{(\rho\sin(\theta)\cos(\varphi) - x)^2 + (\rho\sin(\theta)\sin(\varphi) - y)^2 + (\rho\cos(\theta) - z)^2} \end{aligned} \tag{52}$$

Here $\vec{r}_{obs} = (\rho, \theta, \varphi)$ represents the position of the observer and $\vec{r}_s = (x, y, z)$ yields a point on the circular target screen.

3.6.2. Comparison of first order and second order terms

When using back substitution of the exact phase term the remaining error is estimated by comparing second order against the first order terms.

Expressing R' by $R' \approx \rho - (\vec{r}_{obs} \cdot \vec{r}_s)/\rho$, is valid for $\rho \gg r$, independent of the value $k\rho$, providing an adequate approximation even in the radiating near-field zone [12]. By using $e^{ikR'}/\rho$ instead of $e^{ik\rho}/\rho$ one computes the first order and the second order terms in the Fourier-components of the electrical field:

$\vec{E}^{(1)} \propto k/\rho$ whereas $\vec{E}^{(2)} \propto 1/\rho^2$ and $\vec{E}^{(2)} \propto kr/\rho^2$, with (i), $i = 1, 2$ denoting the respective order. Therefore the second order terms are negligible when $\rho \gg r$ and $k\rho \gg 1$ is valid. In our experimental set-up the typical distance from the radiating target screen (i.e. to the observation plane respectively the first optical element) is 250 mm. For such a distance and frequencies higher than 30 GHz $k\rho \gg 1$ is easily fulfilled. The corresponding electrical field errors for a target screen of radius 28 mm are then estimated to be in the order of 10%. The maximum error is expected to occur normal to the target screen, since at this angle the largest projection of the tilted screen is found. Due to the radially polarized character of TR the intensity must vanish in this symmetrical center. Hence the absolute value of the differences is negligible.

As already mentioned a conservative definition for the Rayleigh distance with $L_R = \frac{4r_s^2}{\lambda}$ is found in classical antenna theory. An alternative definition (IEEE) describes the near-to-far-field boundary by the criteria that the phase of the emitted radiation differs by $\lambda/8$ to the phase of a spherical wave. Both definitions yield Rayleigh distances larger than one meter for a frequency of 120 GHz ($\lambda = 2.5$ mm), proving that the formalism presented here provides a very good approximation for the radiating near-field. Further details are discussed in the next section in conjunction with Fig. 7.

4. Discussion

The introduced analytical model yields a frequency dependent description for the emission process of the long-wavelength TR. In the following the intensity distribution is calculated using our analytical model for a single electron of 100 MeV, which corresponds to the beam energy of the SLS pre-injector LINAC. In Fig. 3 two-dimensional intensity distributions are plotted for three wavelengths: $\lambda = 10.0$ mm (30 GHz), $\lambda = 5.0$ mm (60 GHz) and $\lambda = 2.5$ mm (120 GHz). Hereby the screen has been discretized according to a grid of points (r',ϕ'). The integral was then evaluated as the finite sum over the resulting 4500 grid points. The plots are computed on a plane at a distance $x = 250$ mm. The figures clearly reproduce the expected angular broadening of the emission profile for increasing wavelengths. Furthermore an asymmetry in the emission pattern is observed with respect to the horizontal dimension. Similar to the increased radiation divergence the emission asymmetry is pronounced for longer wavelengths. Fig. 4 shows one-dimensional angular representations of the aforementioned intensity profiles, i.e.

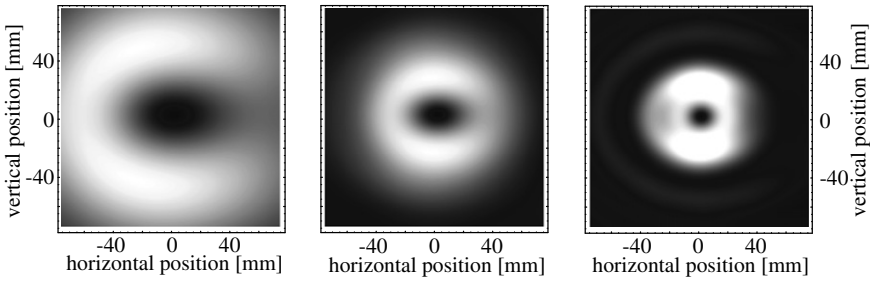

Fig. 3. Computed long-wavelength TR intensity plot (single electron of 100 MeV) for (a) $\lambda = 10.0$ mm, (b) $\lambda = 5.0$ mm and (c) $\lambda = 2.5$ mm on a plane of $x = 250$ mm distance to the circular target screen of radius $r_s = 28$ mm.

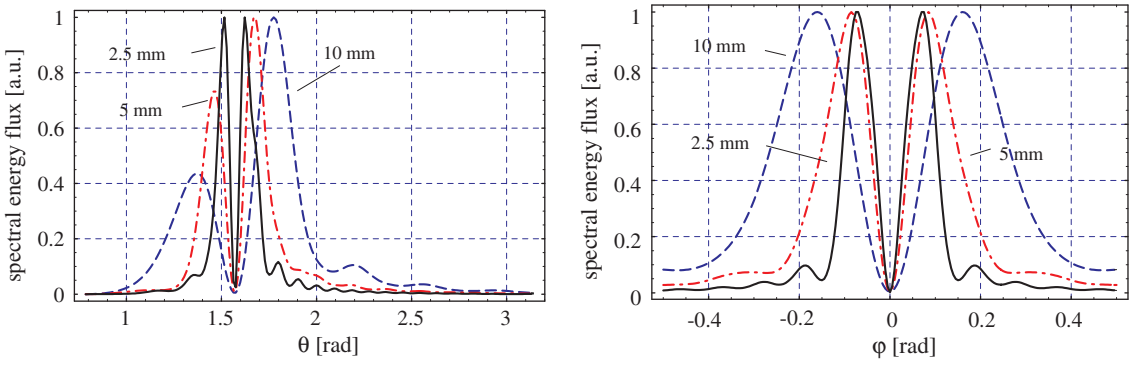

Fig. 4. The calculated long-wavelength TR radiation pattern (single electron of 100 MeV) for a target screen of radius $r_s = 28$ mm at a spherical distance of $R = 250$ mm. Left side: at $\varphi = 0$ (horizontal polarization); Right side: at $\theta = \frac{\pi}{2}$ (vertical polarization). The normalized distribution for three wavelengths is computed: blue line $\lambda = 10.0$ mm, red line $\lambda = 5.0$ mm and black line $\lambda = 2.5$ mm. Left side: the model predicts an emission at $\pi/2$ to the electron beam path with an asymmetry in emission. (For interpretation of the references to colour in this figure, the reader is referred to the web version of this article.)

their corresponding projections on a sphere of 250 mm radius. The horizontal profile is parametrized with θ where as the vertical one is expressed in φ (see Fig. 2). The asymmetry is exclusively apparent in the calculated horizontal intensity profile. For both profiles the maximum in emission occurs at angles much larger than $\frac{1}{\gamma}$ as predicted by the formalism of Ginzburg and Frank for the infinite target size.

These very specific characteristics of the simulated transverse CTR patterns as resulting from the finite-size effects of the target screen have been experimentally confirmed at the SLS LINAC [10,11], for the first time in the coherent long wavelength range. The measurements were conducted using a Golay cell far infrared detector mounted on two motorized linear stages thus allowing two-dimensional scans at a distance $x = 250$ mm to the target screen. The measurements were done for both horizontal and vertical polarization using a wire-grid polarizer in front of the vacuum window of the diagnostic port. For each angular position 30 CTR pulses have been recorded. The dots in Fig. 6 give the mean value, whereas the error bars indicate the corresponding standard deviation due to machine fluctuations. The intensity radiation patterns (bold line) are computed for a discrete set of frequencies and weighted according to the electron bunch power density spectrum as measured with a Martin–Puplett interferometer (MPI) (c.f. Fig. 5). Each horizontal radiation pattern associated to the corresponding spectral line reproduces the distinctive asymmetry. Hence, any spectral superposition must also yield to the asymmetry which points always in the indicated direction. The curves are finally convoluted with the 6 mm aperture of the detector window. The measurements as depicted in Fig. 6 show a good agreement with the theoretical predictions. The asymmetry due to the rotation of the target screen was confirmed for the horizontal profile of the two-lobed emission pattern. It was found that the maximum in emission occurred at an angle of 50 mrad which is a factor 10 larger than the one predicted by Ginzburg and Frank, showing the influence of the finite target size as predicted by the formalism. The underlying power density spectrum used in the simulation has been measured on another occasion with different machine setting of the LINAC. Hence the discrepancies between measurements and simulations can be attributed mainly to deviations in the assumed power density spectrum.

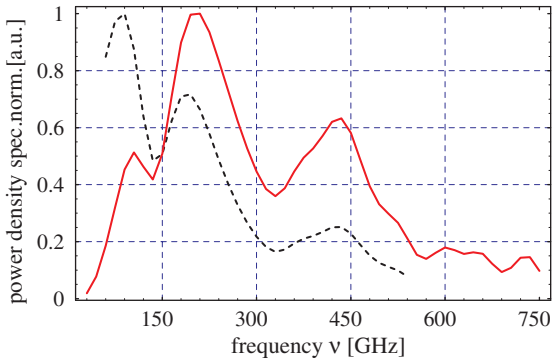

Fig. 5. Measured coherent power density spectrum at the SLS LINAC. The resulting spectrum is in the range of up to 600 GHz. The full line depicts the spectrum as obtained by Fourier transform of the interference profile. The dashed line gives the spectrum as weighted with the transfer function of the interferometer [8]. The latter curve is used for the simulation in Fig. 6.

The emitted radiation is also characterized by its phase front. Fig. 7 gives a comparison between the phase front of a spherical wave and the CTR. It is found that the phase difference of CTR with respect to a perfect spherical wave originating from $\vec{r}_s = (0,0,0)$ is oscillating with a swing of about $\frac{\lambda}{4}$ for the shortest wavelength indicated (2.5 mm). This compares well with the aforementioned alternative definition of the Rayleigh distance at which the mentioned phase difference should amount $\frac{\lambda}{8}$ indicating that the observation point lies within the radiating near-field. The oscillating behavior is attributed to diffraction at the screen boundary. Therefore the emitted long wavelength CTR at this distance can approximated as a spherical wave. The change in sign at $\theta = \frac{\pi}{2}$ respectively at $\varphi = 0$ reproduces the radial polarized character of the emitted CTR.

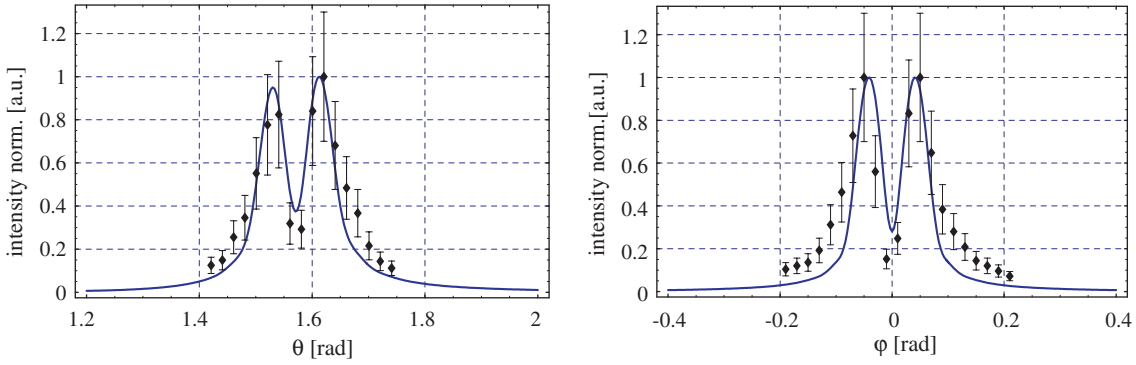

Fig. 6. Measurement of CTR intensity at the SLS LINAC. Left side: horizontal polarization. Right side: vertical polarization. The scans are compared against computed intensity profiles according to the formalism presented in this chapter (full line). The underlying CTR power density spectrum has been measured with an MPI and is shown in Fig. 5.

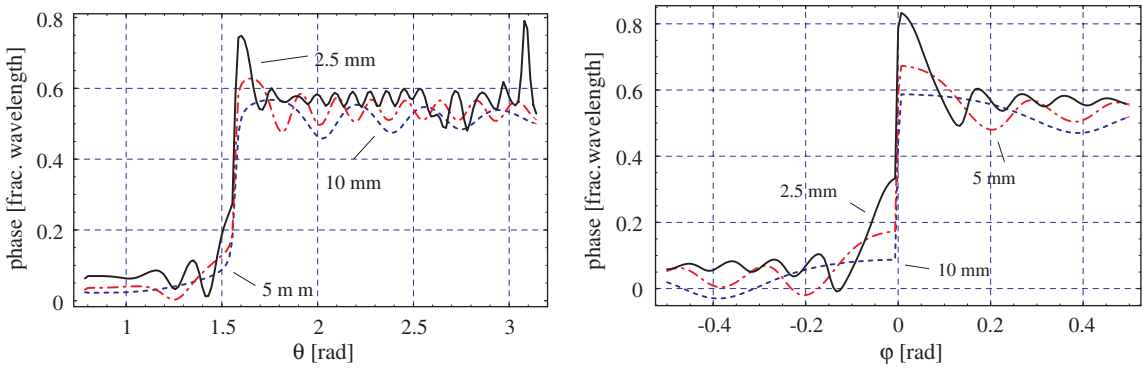

Fig. 7. Computed difference in phase between electric field (left side: θ-component (horizontal polarization) at $\varphi = 0$; right side φ-component (vertical polarization) at $\theta = \frac{\pi}{2}$) of long-wavelength TR (single electron of 100 MeV) and a spherical wave at a distance of $R = 250$ mm for a target screen of radius $r_s = 28$ mm. The phase is shown in fractions of the wavelength, for three different wavelengths: blue line $\lambda = 10.0$ mm, red line $\lambda = 5.0$ mm and black line $\lambda = 2.5$ mm. Note the change in sign at $\theta = \frac{\pi}{2}$, respectively in $\varphi = 0$, indicating the radially polarized character of TR. (For interpretation of the references to colour in this figure, the reader is referred to the web version of this article.)

4.1. Short wavelength limit

In the short wavelength limit the presented CTR emission model correctly merges into the well-known radiation pattern as predicted by the Ginzburg and Frank formalism where the asymmetry in horizontal direction is not apparent and the two radiation lobes are separated by an angle of $2/\gamma$.

In the case of normal incidence the prediction of Ginzburg and Frank can be reproduced analytically. Applying the formalism on the special case of normal incidence the spectral energy in the far-field ($r_s \ll \rho \Rightarrow R = \rho$) is found to be:

$$\frac{d^2I}{d\omega d\Omega} \propto \left(\frac{\left(\frac{\omega}{c}\right)^2}{\gamma}\right)^2 \left| \int_0^{r_s} J_1(\sin(\theta)\frac{\omega}{c}r) K_1\left(\frac{\omega}{\beta\ c\gamma}r\right) r dr \right|^2 \quad (53)$$

where J_1 is the first order Bessel function. The integral can be solved analytically [13]:

$$\frac{d^2I}{d\nu d\Omega} \propto \frac{\beta^2 \sin(\theta)^2}{(1-\beta^2\cos(\theta)^2)^2}[1 - T(\nu,\theta)] \quad (54)$$

using

$$T(\nu,\theta) = \frac{\omega/cr_s}{\beta\gamma} J_0(\omega/cr_s \sin(\theta)) K_1\left(\frac{kr_s}{\beta\gamma}\right) + \frac{kr_s}{\beta^2\gamma^2 \sin(\theta)} J_1(kr_s \sin(\theta)) K_0\left(\frac{\omega/cr_s}{\beta\gamma}\right). \quad (55)$$

The short wavelength limit is tantamount to $r_s \to \infty$ (infinite target screen). Thus, the term $T(\nu,\theta)$ vanishes and the relation of Ginzburg and Frank is revealed in the special case of normal incidence. The radiation pattern displayed in Fig. 8 shows the horizontal intensity profile on a sphere of 1 m radius calculated for the general case of the tilted target screen using formula (51). The asymmetry due to the $\pi/4$ rotation of the target screen with respect to the electrons trajectory is not apparent at these wavelengths and the emission maximum converges to the expected angle $\frac{1}{\gamma}$.

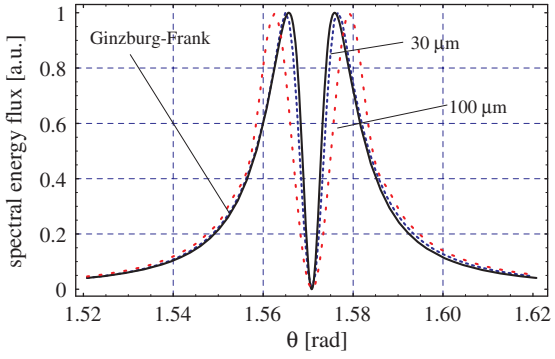

Fig. 8. Calculated intensity distribution (single electron of 100 MeV) for an oblique target screen of radius $r_s = 28$ mm at a spherical distance of $R = 1000$ mm and at $\varphi = 0$. The normalized distribution is computed for the wavelengths: blue line $\lambda = 30.0$ μm, red line $\lambda = 100.0$ μm. The black line presents the prediction of Ginzburg and Frank. (For interpretation of the references to colour in this figure, the reader is referred to the web version of this article.)

At these short wavelengths the source fields impinging on the screen are much smaller than the target size corresponding to the case of the infinite target screen.

5. Summary

The analytical formalism introduced in this paper is rather simple compared to other formalisms [4,5] and numerical codes used for simulations [14]. Nevertheless it covers all cases including the tilted target screen of finite extent, and both the radiating near-field and the far-field and hence, encompassing a wide frequency range. The predicted asymmetry and the angular broadening of the emission was experimentally confirmed. This effects are calculated to occur in the millimeter wavelength range at the SLS pre-injector LINAC (100 MeV). For beam energies of several GeV this behavior must also be taken into account for TR emitted in both the FIR and IR spectral

range. This results from the fact that the transversal extent ($\gamma\lambda$) of the Coulomb source fields is considerably larger than the target dimension at this wavelengths and for such beam energies.

For small wavelengths in the FIR range the model is in agreement with the predictions of Ginzburg and Frank. For the emission from an oblique target screen the characteristic asymmetry in emission vanishes at high frequencies and the two maxima in the emitted energy flux are separated by the well-known angular distance of $2/\gamma$ as obtained by the Ginzburg and Frank formalism.

References

[1] V.L. Ginzburg, I. Frank, Radiation of a uniformly moving electron due to its transition from one medium into another, J. Phys. USSR 9 (1945).
[2] M.L. Ter-Mikaelian, High Energy Electromagnetic Processes in Condensed Media, Wiley, New York, 1972.
[3] C.A. Brau, Modern Problems in Classical Electromagnetics, Oxford Press, New York, 2004.
[4] V.A. Verzilov, Transition radiation in the pre-wave zone, Phys. Lett. A 273 (2000) 135.
[5] S.N. Dobrovolsky, N.F. Shul'ga, Transversal spatial distribution of transition radiation by relativistic electron in the formation zone by the dotted detector, Nucl. Instr. and Meth. B 201 (2003) 123.
[6] V.L. Ginzburg, Applications of Electrodynamics in Theoretical Physics and Astrophysics, Gordon and Breach Science Publishers, Amsterdam, 1989.
[7] B. Borden, Mathematical problems in radar inverse scattering, Inst. Phys. Publishing, Inverse Problems 18 (2001) R1.
[8] D. Sütterlin, Single-Shot Electron Bunch-Length Measurements with a Spatial Electro-Optical-Auto-Correlation-Interferometer using Coherent Transition Rradiation at the 100 MeV SLS Pre-Injector LINAC, Ph.D. thesis, No. 16668 submitted to the Swiss Federal Institute of Technology, Zurich ETHZ (2006).
[9] J.B. Rosenzweig, S. Reiche, Transition radiation for uneven, limited surfaces, in: Proceedings PAC-01 (Chicago, United States 2001).
[10] D. Sütterlin, V. Schlott, H. Sigg, H. Jäckel, Developement of a Bunch-Length Monitor with Sub-Picosecond Time Resolution and Single-Shot Capability, in: Proceedings DIPAC-03 (Mainz, Germany 2003).
[11] D. Sütterlin, V. Schlott, H. Sigg, D. Erni, H. Jäckel, A. Murk, Spatial auto-correlation interferometer with single shot capability using coherent transition radiation, in: Proceedings DIPAC-05 (Lyon, France 2005).
[12] J.D. Jackson, Classical Electrodynamics, Second ed., Wiley, New York, 1975.
[13] P. Schmueser, B. Schmitt, S. Casalbuoni, Far-infrared transition and diffraction radiation, TESLA Report 2005-15 (Tesla Test Facility, DESY Hamburg 2005).
[14] S. Casalbuoni, THz generation and transport, talk at ICFA Future Light Sources Subpanel Miniworkshop on XFEL Short Bunch Measurement and Timing (Stanford Linear Accelerator Center, United States 2004).